Research on Chemical Intermediates (2022) 48:1129–1150
https://doi.org/10.1007/s11164-021-04626-0

Cobalt promoted Ni/$MgAl_2O_4$ catalyst in lean methane catalytic oxidation

Mohammad Varbar[1] · Seyed Mehdi Alavi[1] · Mehran Rezaei[1] · Ehsan Akbari[1]

Received: 23 August 2021 / Accepted: 4 November 2021 / Published online: 22 November 2021

Abstract

In the present research, magnesium aluminate spinel was prepared as catalyst support using a novel, facile, and efficient mechanochemical method. The Co-promoted catalysts with 20 wt.% of Ni were fabricated using an impregnation route and the samples were analyzed by the X-ray diffraction (XRD), N_2 adsorption/desorption (BET), temperature-programmed reduction and desorption (H_2-TPR and O_2-TPD), and field emission scanning electron microscopy (FESEM) tests. The results confirmed that all samples have a mesoporous structure with a high specific surface area and the presence of cobalt caused complete CH_4 oxidation at low temperatures, and no side reactions were observed. The results indicated that the 3%Co-20%Ni/$MgAl_2O_4$ catalyst was the optimal sample among the prepared catalysts, owing to the improvement of reduction features and oxygen mobility. The 50 and 90% of methane conversion was obtained at 530 and 600 °C, respectively. Also, the influence of calcination temperature, GHSV, and feed ratio was determined on the catalytic activity. The obtained outcomes revealed that the calcination temperature has a significant effect on the textural properties and catalytic efficiency. The sample calcined at 700 °C showed the weakest performance, which was related to the sintering of particles at high temperatures. The catalytic stability showed that the 3%Co-20%Ni/$MgAl_2O_4$ has acceptable stability during 600 min time of reaction.

✉ Seyed Mehdi Alavi
alavi.m@iust.ac.ir

✉ Mehran Rezaei
mrezaei@iust.ac.ir

[1] Faculty of Chemical, Petroleum and Gas Engineering, Iran University of Science and Technology, Tehran, Iran

Graphical abstract

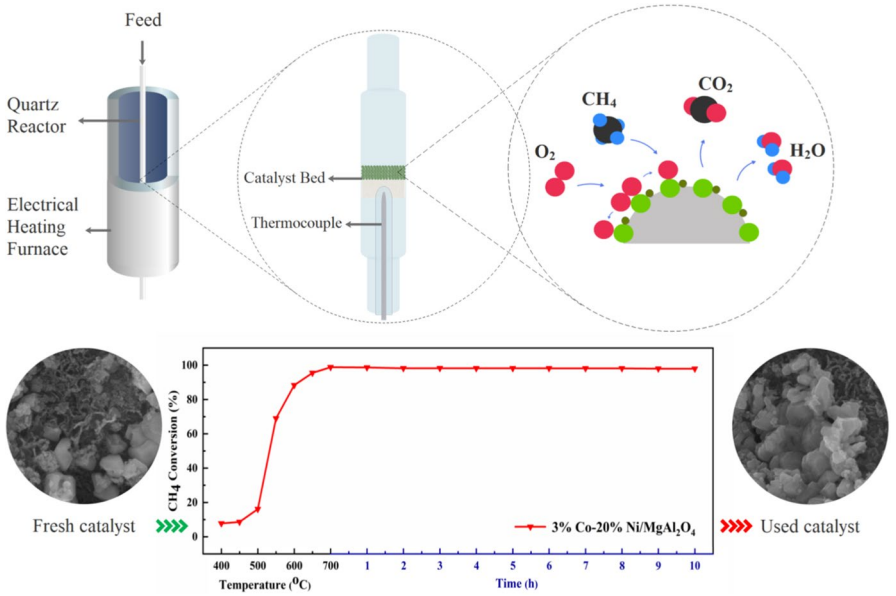

Keywords Methane catalytic oxidation · Light-off temperature · Mechanochemical · Transition metals · Co–Ni/$MgAl_2O_4$ · Cobalt–Nickel catalyst

Introduction

Energy supply is one of the main issues of economic development. Despite the increasing energy demand and the development of renewable energy, fossil fuels (coal, oil, and natural gas) are still substantial. A significant part of this energy is supplied from the combustion of natural gas [1]. Natural gas is chiefly formed of CH_4 and is one of the most important fossil fuels due to its higher energy content and lower carbon dioxide emissions [2]. The temperature of the non-catalytic combustion reaction is about 1300–1400 °C, which causes the release of harmful pollutants such as NO_x, CO, and unburned hydrocarbons [3]. Therefore, reducing the emission of these pollutants is necessary for economic and environmental goals [4]. Catalytic oxidation of methane is a promising technology to reduce combustion pollutants and rational use of fossil fuels [5, 6].

According to previously published literature, different types of catalysts have been reviewed for the complete catalytic combustion of methane, such as noble metals [7, 8], perovskites [9, 10], spinels [11], hexaaluminates [12], and transition metal oxides [13, 14]. Among them, catalysts containing noble metals (Pd, Pt, Au, Rh) have been more studied. These metals are very active in the oxidation process at low temperatures. However, the high cost of precious metals limits their practical use

on a large scale. As a result, we need to develop suitable catalysts with high activity and stability. It was observed that the transition metals show acceptable activity at relatively low temperatures for methane oxidation [15]. Nickel-based catalysts are usually utilized in the oxidation–reduction process as efficient catalysts due to their superior activation ability for breaking C–H and H–H bonds [16]. Previous studies have shown that the addition of NiO to other components can improve the redox properties and oxygen storage capacity, which can lead to the higher activity of these catalysts [17]. Although many attempts have been performed to prepare a catalyst with high efficiency in the methane oxidation reaction, a catalyst that can significantly reduce the light-off temperature and increase the catalyst stability has become a challenge. In other words, the use of compounds that enhance oxygen mobility is essential in catalyst formulation. Among the various metals, Co_3O_4 is a suitable catalyst for methane combustion [18]. Cobalt oxides have been obtained using various precursors and different preparation methods such as direct thermal decomposition [19], hydrothermal [20], and combustion [21]. The published reports indicated that the catalytic efficiency of the catalysts was related to the combustion behavior of cobalt precursors and fuels [22]. The performance of cobalt oxide on various supports such as MgO [23], Al_2O_3, ZrO_2, TiO_2 [24], CeO_2 [25] has been investigated. However, at temperatures above 550 °C, the performance of the catalyst decreased due to the agglomeration. The use of supports can stabilize the cobalt particles on the catalyst surface and minimize the degree of agglomeration [22]. However, magnesium aluminate spinel can be considered as potential catalyst support to stabilize and prevent the sintering of cobalt particles at high temperatures [26].

Magnesium aluminate ($MgAl_2O_4$) has been extensively studied in various processes such as glycerol steam reforming [27], methane decomposition [28], methane steam, and dry reforming [29–32], autothermal reforming [33], and methane catalytic combustion [34]. The high melting temperature, high stability, low density, and good optical and catalytic properties are its most critical unique features [35, 36].

There are various methods for synthesizing $MgAl_2O_4$, such as co-precipitation [37], sol–gel [38], combustion [39], hydrothermal [40], and mechanochemical [41]. As known, the use of catalysts with high specific surface area is essential in oxidation reactions. However, some of the mentioned preparation methods are complicated and high cost, which make the scale-up of the process difficult. Furthermore, in the common preparation methods, the use of the high temperature solid-state reactions is necessary to obtain the spinel phase, which leads to decreasing the porosity and specific surface area. The low porosity and BET area limit the use of the prepared spinel powders in catalytic applications. Among the synthesis methods, the precipitation and sol–gel can be considered as the potential methods for the preparation of the spinel powders with a high surface area at low temperatures. However, the precipitation method is complex and it requires the precious control of the synthesis parameters such as pH, temperature, aging time, molarity, etc. In the sol–gel process, the metal alkoxides are usually employed, which are expensive and cannot be used on an industrial scale.

Meanwhile, the mechanochemical synthesis method is one of the innovative synthesis methods due to the simplicity and the use of conventional precursors. Compared to the general preparation methods, the mechanochemical route is

environmentally friendly and is performed at room temperature. On the other side, this method is known as the fast preparation route due to reducing the number of operation steps. Furthermore, the produced nanomaterials by the mechanochemical method have outstanding features such as small crystallite size, uniform shape, and morphology with a low degree of agglomeration, narrow pore size distributions, etc. [42]. In this study, $MgAl_2O_4$ spinel with small crystal size, high surface area, and suitable porosity was prepared by the mechanochemical method and applied as a support for Ni and Co-based catalysts in methane catalytic combustion. There are few articles on the use of $MgAl_2O_4$ as catalyst support in the methane oxidation process.

Experimental

Catalyst preparation

$Mg(NO_3)_2.6H_2O$, $Al(NO_3)_3.9H_2O$, $Ni(NO_3)_2.6H_2O$, $Co(NO_3)_2.6H_2O$ (Merck, 99%), and $(NH_4)_2CO_3$ (LOBA CHEMIE, 98%) were used as raw materials.

The catalyst support ($MgAl_2O_4$) was synthesized using the solid-state mechanochemical synthesis method with a stoichiometric ratio of $MgO:Al_2O_3 = 1:1$. For each gram of the support, 1.8 g magnesium nitrate hexahydrate, 5.3 g aluminum nitrate nonahydrate, and 5.3 g ammonium carbonate were combined in a ceramic agate mortar at ambient temperature to prepare a pasty solid. The mechanochemical synthesis method is similar to the precipitation method, except that the crystallization water released by the mechanical force during the milling process can act as the solvent during the synthesis process. This method eliminates the need for solvent during the process and consequently generates no waste. During the preparation process, ammonium carbonate, as a precipitating agent, was dissolved in the crystallization water and caused the precipitation of the metal nitrate precursors by increasing the pH value. Then, the wet cake was dried at 110 °C for 24 h, and calcined at 600 °C (3 °C/min).

The nickel and cobalt were loaded on the catalyst support by the wet impregnation method. In this study, the nickel content was remained constant at 20 wt.%, and the cobalt loading was varied from 1 to 7 wt.%. Then, the sample was dried at 110 °C for 24 h and eventually calcined at 600 °C for 3 h. The obtained catalysts were denoted as x%Co-20%Ni/$MgAl_2O_4$ and x demonstrates the weight percentage of cobalt oxide. A schematic diagram of the catalyst preparation is displayed in Fig. 1.

Catalyst characterization

XRD, BET, TPR, O_2-TPD, and FESEM techniques were utilized to specify the physicochemical features of the prepared catalysts. The crystalline structure of the calcined samples was evaluated using a PANalytical X'Pert-Pro instrument equipped with a Cu-Kα radiation source ($\lambda = 1.5486$). The specific surface area, pore volume,

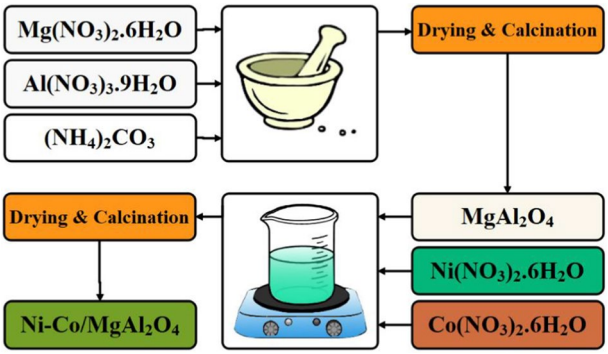

Fig. 1 Schematic diagram of the catalyst preparation method

and pore size distribution of the calcined catalysts were determined by the nitrogen physisorption at 77 K using a Belsorp Mini II device. In this analysis, 100 mg of the sample was first degassed at 250 °C for 2 h under vacuum. The BET surface area was measured in the relative pressure range of 0.02–0.3, assuming 0.1620 nm^2 for nitrogen cross-sectional area. To evaluate the reducibility of the fresh catalysts, H_2-TPR analysis was done in a quartz reactor connected to a thermal conductivity detector (TCD) with 5% H_2 diluted in Ar gas (20 cc/min). Before the test, 100 mg of the calcined catalyst was degassed at 250 °C for 2 h, and then the temperature decreased to room temperature. Finally, the H_2-TPR analysis was performed from 50 up to 700 °C with a heating rate of 10 °C/min. O_2-TPD analysis was performed to survey the oxygen mobility of the calcined catalysts with the same instrument as explained for H_2-TPR analysis. 300 mg of the samples were pretreated at 250 °C for 2 h under vacuum. Then, the catalyst was oxidized with 15 cc/min oxygen flow for 45 min. The stream was switched to helium gas (15 cc/min) for 15 min to remove the physically adsorbed oxygen. The desorption was conducted from room temperature to 800 °C under a pure helium stream with a heating rate of 10 °C/min. The morphology of the fresh and used catalysts was studied using the FESEM analysis by a MIRA3 TESCAN instrument at the acceleration voltage of 10 kV.

Catalytic tests

The CH_4 catalytic oxidation process was performed in a quartz tubular flow microreactor with 70 cm length and an inside radius of 0.4 cm at ambient pressure. The catalyst particles (0.2 g, 300–600 µm) were placed in the middle of the reactor on quartz wool, and a thermocouple (K-type) and a programmable thermometer (Hanyoung PX9) were applied to measure and control the catalyst bed temperature. The inlet gas flow consisted of methane, oxygen, and argon (molar ratio = 1:6:7) with a gas hourly space velocity (GHSV) of 24,000 $cm^3/h.g_{cat}$ was passed over the catalytic bed. Parker mass flow controllers were used to adjust the input flows. Before the activity test, the prepared catalysts were pretreated under the oxygen flow at 400 °C for 1 h. The test was performed in the temperature range of 400–700 °C with

intervals of 50 °C. Three injections were carried out at each temperature for repeatability. The reactor outlet gas mixture was sequentially analyzed with a gas chromatograph (Younglin YL 6100) outfitted with a Carboxen 1010 column and a micro TCD detector. A schematic diagram of the experimental setup is shown in Fig. 2. The CH_4 conversion was calculated using the following equation (Eq. 1).

$$X_{CH_4}\% = \frac{X_{CH_{4_{in}}} - X_{CH_{4_{out}}}}{X_{CH_{4_{in}}}} \times 100 \quad (1)$$

where C_{CH4in} is the input methane concentration and C_{CH4out} is the output methane concentration.

Results and discussion

Structural properties of the x%Co-20%Ni/$MgAl_2O_4$ catalysts

Figure 3 displays the XRD patterns of the catalysts prepared with different cobalt loadings. As can be observed, there are various diffraction peaks related to $MgAl_2O_4$, NiO, and Co_3O_4. The diffraction peaks located at $2\theta = 19.03°$, 31.3°, 36.8°,44.8°, 59.3°, and 65.2° are assigned to the spinel phase of $MgAl_2O_4$, and the diffraction peaks observed at $2\theta = 43.3°$, and 62.9° are related to the NiO diffraction crystalline phase [43–45]. The diffraction peaks at $2\theta = 31.5°$, 37°, 43.3°,44.8°, 59.5°, 62.8°, and 65.1° are related to the Co_3O_4 [46]. However, a substantial overlap was observed among the diffraction peaks of the $MgAl_2O_4$, NiO, and Co_3O_4 phases.

Furthermore, these patterns confirmed that the addition in cobalt content intensified the diffraction peaks related to the Co_3O_4 phase, indicating the

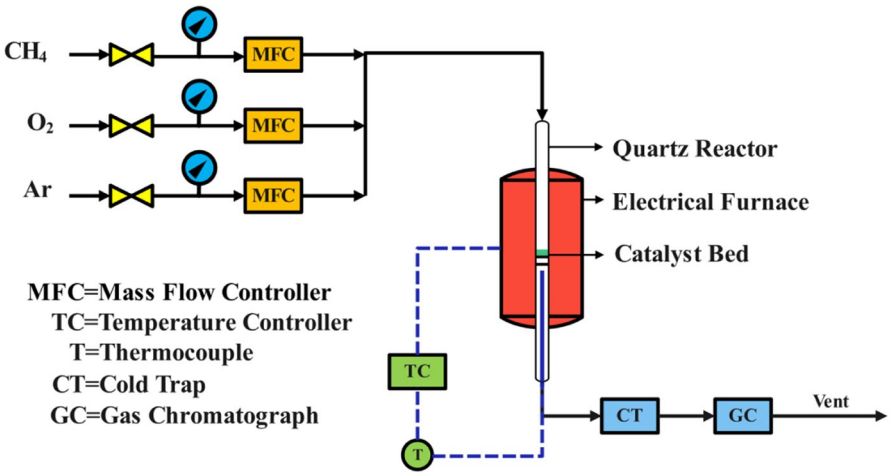

Fig. 2 Schematic diagram of the experimental setup

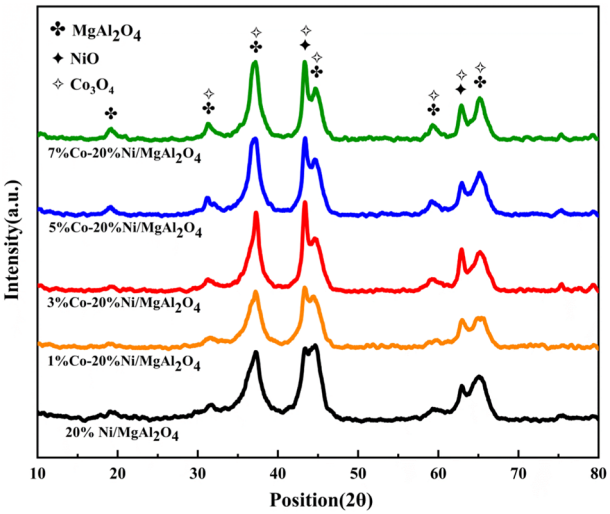

Fig. 3 XRD patterns of the x%Co–20%Ni/$MgAl_2O_4$ catalysts calcined at 600 °C

increase in the crystallite size and decreasing the dispersion of cobalt oxide on the surface of the catalyst.

Figure 4a shows the nitrogen adsorption–desorption isotherms of the synthesized samples. All calcined catalysts show the type IV isotherm, which is the characteristic of the materials with mesoporous structures. The type of the hysteresis loop is H3, which indicates the presence of mesopores with a slit-like shape [47].

The pore size distribution shown in Fig. 4b illustrated that all samples exhibited a pore size in the range of 1–10 nm, and the rise of cobalt loading did not alter the pore size distribution. Table 1 reports the structural characteristics of the catalysts containing cobalt promoters. This table showed that all samples have a nanocrystalline structure with a high specific surface area. Also, with rising cobalt percentage, the BET area and pore volume decreased, which is compatible with the increase in crystallite size observed in the XRD results. Moreover, the crystallite size determined using the Scherrer equation (Eq. 2), revealed that the increment in weight percentage of cobalt increased, the mean crystallite size of the synthesized catalysts from 3.2 to 3.8 nm.

$$D = \frac{k\lambda}{\beta \cos\theta} \tag{2}$$

In this equation, k is a dimensionless shape factor (0.9), $\lambda = 1.54$ is the X-ray wavelength, β is the line broadening at half the maximum intensity (FWHM), and θ is the Bragg angle.

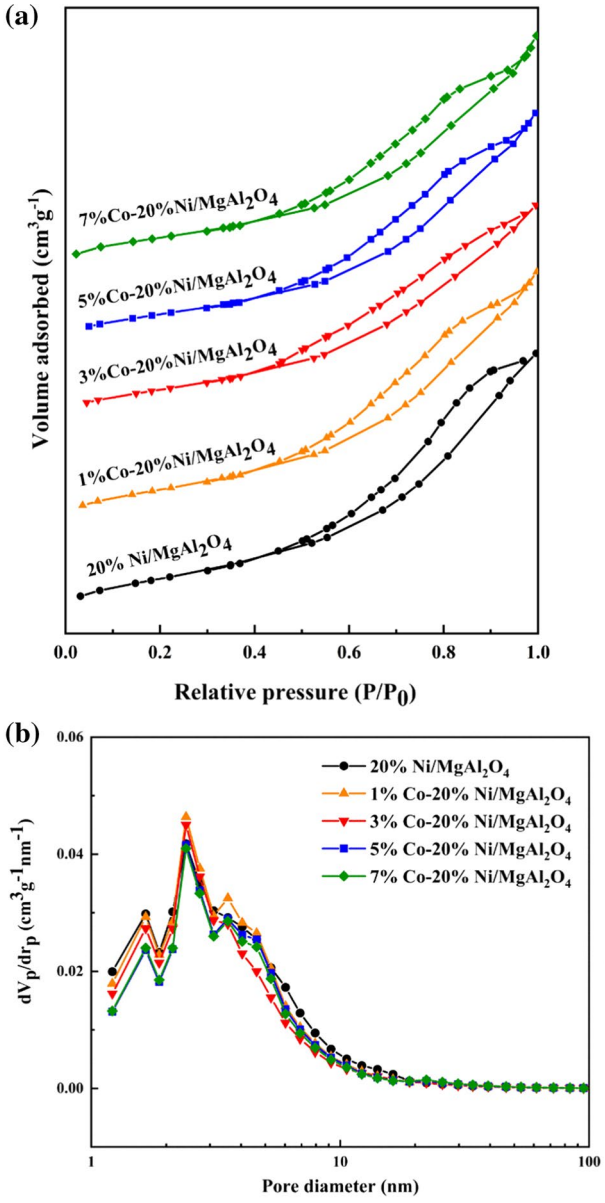

Fig. 4 **a** N_2 adsorption–desorption isotherms and **b** pore size distribution profiles of the x%Co–20%Ni/$MgAl_2O_4$ catalysts calcined at 600 °C

Temperature-programmed analysis of the x%Co-20%Ni/$MgAl_2O_4$ catalysts

H_2-TPR analysis was carried out to identify the reduction characteristics of the catalysts with various cobalt contents, and the obtained profiles are shown in

Table 1 Structural properties of the x%Co–20%Ni/$MgAl_2O_4$ catalysts calcined at 600 °C

Sample	SBET ($m^2\ g^{-1}$)	Pore volume ($cm^3\ g^{-1}$)	Pore size (nm)	Average crystallite size (nm)
1%Co-20%Ni/MgAl2O4	98	0.212	8.74	3.2
3%Co-20%Ni/MgAl2O4	88	0.195	8.82	3.5
5%Co-20%Ni/MgAl2O4	84	0.194	9.37	3.6
7%Co-20%Ni/MgAl2O4	80	0.191	9.59	3.8

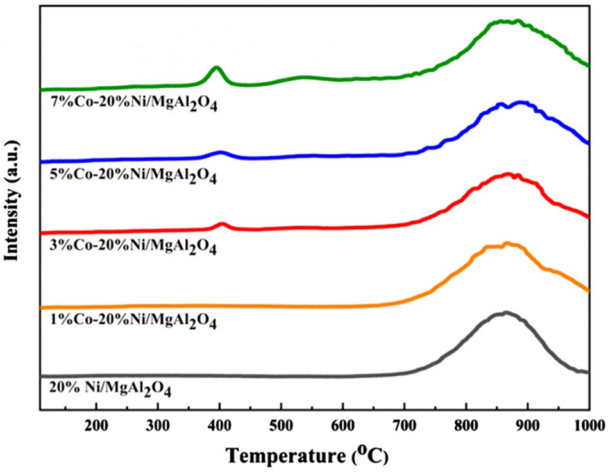

Fig. 5 H_2-TPR profiles of the x%Co–20%Ni/$MgAl_2O_4$ catalysts calcined at 600 °C

Fig. 5. For unpromoted catalyst, there was one reduction peak in the temperature range of 700–1000 °C, which was attributed to the reduction of nickel oxide varieties with a powerful interaction with the support [48]. However, the addition of 1wt.% of cobalt did not change the reduction pattern due to the low amount of cobalt loading. Similar patterns of hydrogen consumption were observed for other promoted samples. The low-temperature reduction peak at about 400 °C could be assigned to the reduction of cobalt oxide species [49]. Furthermore, the intensity of the low-temperature reduction peak increased with increasing in cobalt contents from 3 to 7 wt.%.

O_2-TPD analysis was accomplished to study the activation and oxygen mobility on the catalyst surface and the role of surface O_2 species in the methane catalytic combustion, and the results are shown in Fig. 6. Oxygen mobility plays a crucial role in methane catalytic oxidation. In the samples containing cobalt (except 1wt.% Co), two active desorption peaks were detected. The weak peak at low temperatures is mainly caused by the adsorption of adsorbed O_2 on the catalyst surface, indicating the presence of oxygen vacancies on the catalyst surface. The desorption peak at high temperatures was attributed to the excretion of non-stoichiometric oxygen from the crystal lattice and cobalt oxide reduction. As

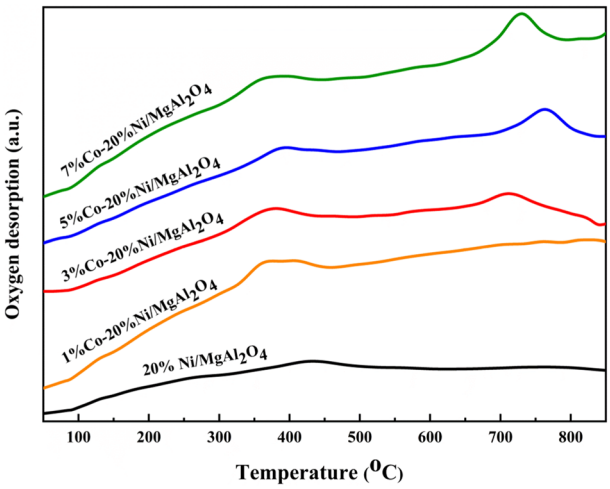

Fig. 6 O_2-TPD profiles of the x%Co-20%Ni/$MgAl_2O_4$ catalysts calcined at 600 °C

can be observed, with raising the cobalt content, the intensity of excretion peaks increased, which could have a positive effect on the catalyst activity. On the other hand, with increasing the cobalt content higher than 3wt.%, the oxygen desorption peaks are transferred to higher temperatures, which displays the decline in the rate of oxygen mobility in samples with higher cobalt contents [50].

Catalytic performance of the x%Co-20%Ni/$MgAl_2O_4$ catalysts

The effect of various cobalt contents on the catalytic activity of x%Co-20%Ni/$MgAl_2O_4$ in the lean methane catalytic oxidation under oxygen-rich was investigated, and the consequences are revealed in Fig. 7. Furthermore, the blank test was performed and the obtained results are revealed in this figure. The indicated results showed that the combustion efficiency was very low in the absence of a heterogeneous catalyst. The presence of cobalt resulted in the elimination of side reactions and the complete oxidation of methane at all temperatures. However, doping of 1wt.% of cobalt oxide did not significantly change the methane conversion due to the low content of cobalt oxide. The presence of higher percentages of cobalt up to 3 wt.% improved the catalytic activity. The 3%Co-20%Ni/$MgAl_2O_4$ possessed the best performance in methane combustion at low temperatures due to the high oxygen mobility, which is in agreement with the obtained results from the textural features. It was reported that the number of active sites was related to the distribution of the active components on the support. Increasing the percentage of the active components lessened the dispersion rate and thus reduced the number of active catalytic sites. Therefore, there is an optimum value for the cobalt content, in which the catalyst has the maximum efficiency [43]. Therefore, 3%Co-20%Ni/$MgAl_2O_4$ was the optimum catalyst that reduced the light-off temperature about 50 °C.

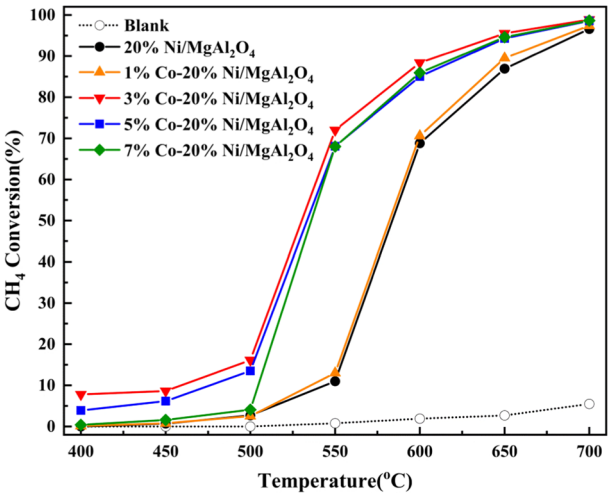

Fig. 7 CH_4 conversion of the x%Co–20%Ni/$MgAl_2O_4$ catalysts calcined at 600 °C. Reaction conditions: 7% CH_4 and 42% O_2 balanced with Ar; GHSV = 24,000 (ml/h g_{cat})

Influence of operating conditions on the catalytic performance of the 3%Co-20%Ni/$MgAl_2O_4$ catalyst

The methane catalytic stability of the 3%Co-20%Ni/$MgAl_2O_4$ at 700 °C for 600 min was studied with a GHSV value of 24,000 (ml/h.g_{cat}), and the obtained results are presented in Fig. 8. No adverse reactions occurred during the stability test. It is known that agglomeration and carbon formation are two important factors in catalyst

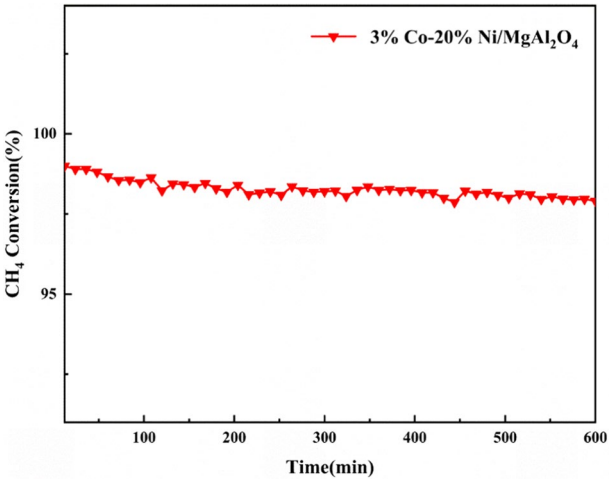

Fig. 8 CH4 conversion stability of the 3%Co–20%Ni/MgAl2O4 catalyst at 700 °C. Reaction conditions: 7% CH_4 and 42% O_2 balanced with Ar; GHSV = 24,000 (ml/h gcat)

deactivation. It has also been reported that nickel-containing magnesium aluminate catalysts have suitable catalytic performance due to their resistance against physical degradation, but coke formation slightly reduces catalytic performance [5]. It has been reported that coke deposition occurred on the catalyst surface in the feed with a CH_4 concentration above 26.5 vol% (Volumetric percentage). Hence, based on our applied reaction conditions, this insignificant decline in CH_4 conversion was just because of the sintering of the active phase during the reaction [51].

To investigate the morphology of the fresh and used 3%Co-20%Ni/$MgAl_2O_4$ catalyst, FESEM analysis was performed, and the obtained images are shown in Fig. 9a and b. It has been observed that the fresh catalyst was composed of agglomerated particles and the used catalyst also showed the same morphology as the fresh catalyst. Figure 10 displays the N_2 adsorption/desorption isotherms of the samples before and after the stability test. It is shown that no observable change was seen in the isotherm shape and pore size distribution. The textural properties of the catalyst before and after the stability test are presented in Table 2. As can be observed, the BET surface area and pore volume of the catalyst reduced after the stability test, while the pore size was raised. This phenomenon is owning to the agglomeration and sintering of particles after the 600 min time on stream.

Based on the published articles, changing the feed molar ratio can affect the activity of different samples because the selectivity of products in the catalytic oxidation of methane is strongly dependent on the O_2 to CH_4 molar ratio. For this purpose, the performance of 3%Co-20%Ni/$MgAl_2O_4$ catalyst as the best sample was investigated under different feed ratios at 600 °C and under a GHSV value of = 24,000 ml/h.g_{cat}. Also, the total input feed is 80 ml/min, half of which was argon. As shown in Fig. 11, the methane conversion reduced with increasing the O_2 to CH_4 molar ratio due to the competitive adsorption among adsorbed CH_4 and O_2 varieties. The lower conversion rate of CH_4 at higher ratios could be described by the fact that more O_2

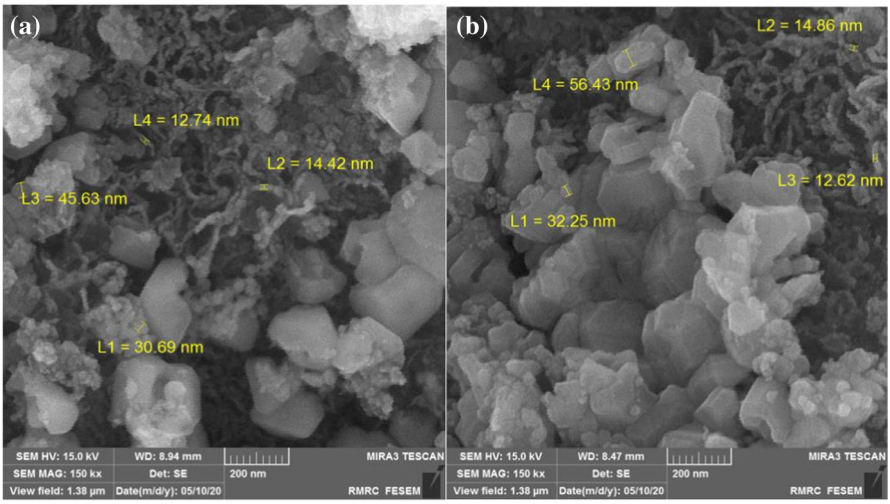

Fig. 9 FESEM images of the **a** fresh and **b** used 3%Co-20%Ni/$MgAl_2O_4$ catalyst

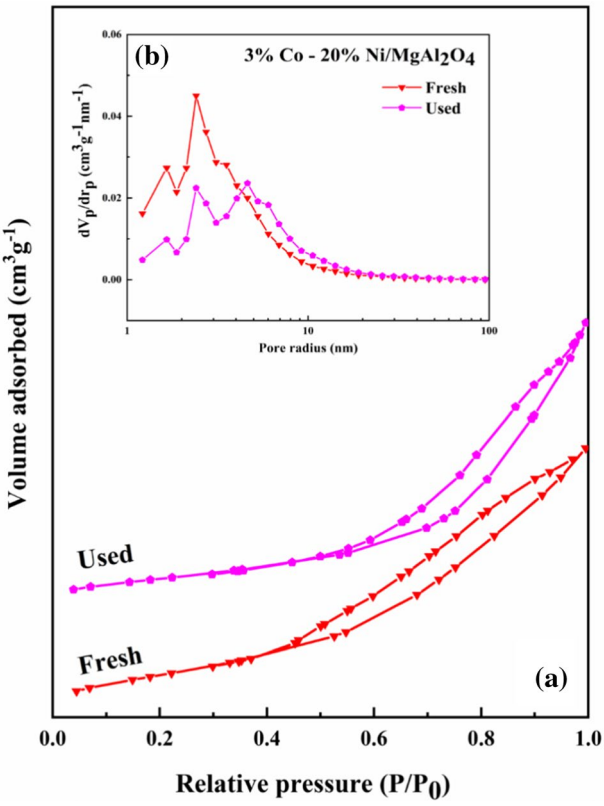

Fig. 10 **a** N_2 adsorption–desorption isotherms and **b** pore size distribution profiles of the fresh and used x%Co–20%Ni/$MgAl_2O_4$ catalyst

Table 2 Structural properties of the fresh and used 3%Co–20%Ni/$MgAl_2O_4$ catalyst

Sample	SBET ($m^2\ g^{-1}$)	Pore volume ($cm^3\ g^{-1}$)	Pore size (nm)
Fresh	88	0.195	8.82
Used	57	0.187	13.30

varieties were absorbed and repressed the CH_4 adsorption due to the more adsorption energy of methane which reduced the methane conversion[52].

Figure 12 displays the effect of gas hourly space velocity variation on the methane conversion in 3%Co-20%Ni/$MgAl_2O_4$ catalyst at 600 °C under a CH_4:O_2:Ar = 1:6:7. According to the obtained results, the methane conversion increased with the rising of GHSV value from 18,000 to 42,000 mL/h.g_{cat}.

It is theoretically known that at lower space velocities, the reactants have more time to access the active sites of the catalyst, which caused more methane molecules to be adsorbed. Generally, the CH_4 conversion depends on the inherent kinetics of

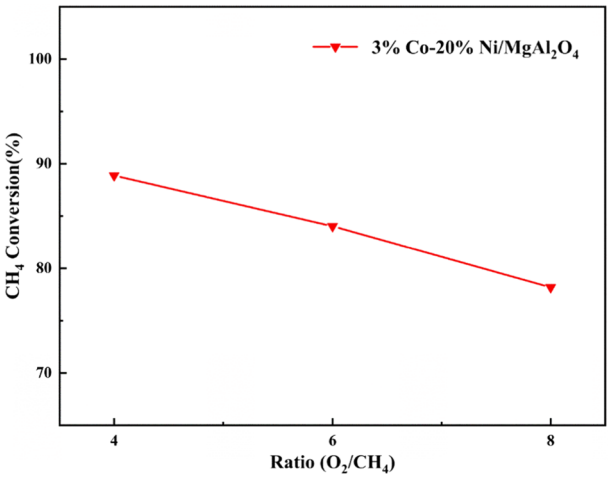

Fig. 11 Influence of O_2/CH_4 molar ratio on the catalytic activity of the 3%Co–20%Ni/$MgAl_2O_4$ catalyst at 600 °C

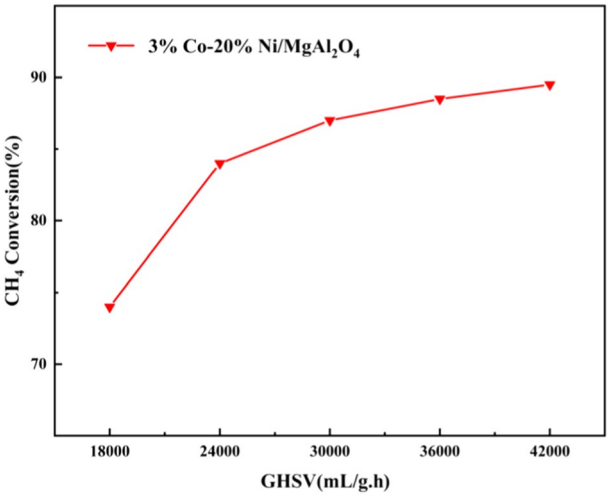

Fig. 12 Influence of GHSV on the catalytic activity of the 3%Co–20%Ni/$MgAl_2O_4$ catalyst at 600 °C

the reaction and mass transfer. Internal mass transfer appertains largely on the features of the catalyst (including penetration of pores and their size and volume). The external mass transfer from the gas phase to the surface of the catalyst is restricted via the residence time, i.e., the flow rate of the reactants. Also, in exothermic reactions, the temperature gradient affects the reaction rate [6, 53]. On the other hand, rising GHSV value is also effective in reducing the residence time of reactants on the surface of the catalyst. In this regard, the exothermic reaction causes a higher temperature gradient in the catalyst bed. Also, increasing the velocity and amount

of reactants enhances the transfer of external mass. These two factors are effective in increasing methane conversion in higher GHSVs and have overcome the factor of reducing residence time. Also, according to reports, by increasing the space velocity at an appointed temperature, a steady-state conversion rate can be obtained, after which, raising the velocity did not affect the methane conversion rate. Therefore, the mass transfer limiting factor at higher space velocities is negligible. This is confirmed by decreasing the slope of the graph at a higher space velocity [6, 53]. Thus, releases of the heat from the catalyst bed can enhance the temperature of the bed, and consequently, the reaction proceeds toward the CH_4 oxidation. Consequently, there is an appropriate ratio between the GHSV value and CH_4 conversion, which should be regulated for a specific application.

The impact of feed dilution on the catalytic performance over the 3%Co-20%Ni/$MgAl_2O_4$ catalyst with a $O_2/CH_4 = 6$, methane, and oxygen input feed at GHSV = 12,000 mL/h.g_{cat} and argon diluent at 600 °C was investigated, and the results are demonstrated in Fig. 13. As shown in this figure, methane conversion decreased with increasing argon flow rate from 12,000 to 72,000 mL/h.g_{cat}. In this section, by keeping the content of reactants at a constant value and expanding the argon flow, the effect of the exothermic reaction and the amount of input methane is eliminated. Increasing the argon flow and diluting the feed reduced the residence time of the reactants and their adsorption on the catalyst surface, thereby reducing the methane conversion rate.

Influence of calcination temperature

The influence of the calcination temperature on the structure and catalytic activity of the optimal sample was studied and the results are presented in this section.

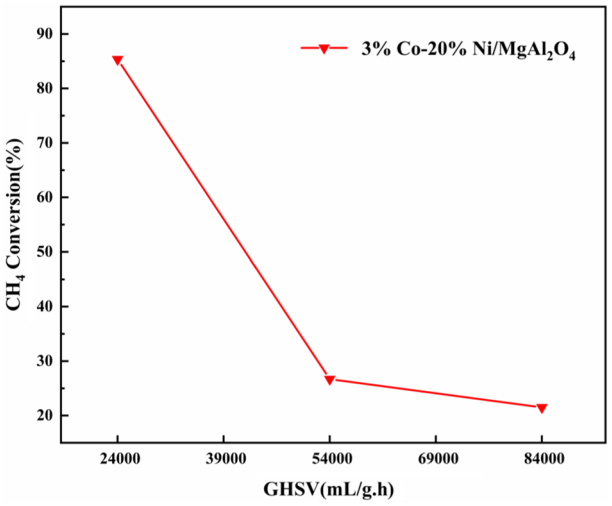

Fig. 13 Influence of feed dilution on the catalytic activity of the 3%Co-20%Ni/$MgAl_2O_4$ catalyst at 600 °C

XRD diffraction patterns of the 3%Co-20%Ni/$MgAl_2O_4$ catalysts calcined at various temperatures are displayed in Fig. 14. It is shown that the change of calcination temperatures did not cause to formation of a new phase in the catalyst. Furthermore, increasing the calcination temperatures from 500 to 700 °C leads to an enhancement in the intensity of diffraction peaks, indicating an increase in crystallite size of the catalysts calcined at higher temperatures [54]. Therefore, the largest crystal size was found in the catalyst calcined at 700 °C.

Figure 15a displays the N_2 adsorption–desorption isotherms of the catalysts calcined at different temperatures. For all calcined catalysts, type IV isotherm is observed, which belongs to the materials with mesoporous structures, and conforming to IUPAC classification, the formed hysteresis belonged to the H3 type. This kind of hysteresis loop has ordinarily appeared on the bulk or lump solids, with slit-shaped pores (particles with edges or plates like a cube) with non-uniform size and shape. Increasing the calcination temperature results in a decline in the width of the hysteresis loop, which indicates a reduction in the BET area and the destruction of the mesopore structure [47, 54].

Figure 15b also shows the pore size distribution patterns of the calcined catalysts at different temperatures and confirmed the existence of the mesopore structures. Increasing the calcination temperature shifts the pore size distributions to larger values, which may be due to the destruction of pores at higher temperatures [54].

Table 3 reports the structural characteristics of the calcined samples at different temperatures. As can be seen, all samples have a nanocrystalline structure with a high specific surface area. The volume and diameter of the pores increased with raising the calcination temperature. The outcomes also exhibited that with raising the calcination temperature, due to the particle clumping, the collapse of the pores structure, and particle compaction, the size of crystalline particles

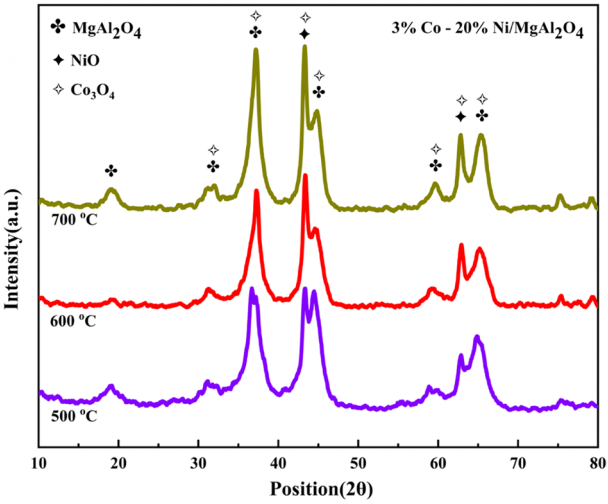

Fig. 14 XRD patterns of the 3%Co–20%Ni/$MgAl_2O_4$ catalysts calcined at various temperatures

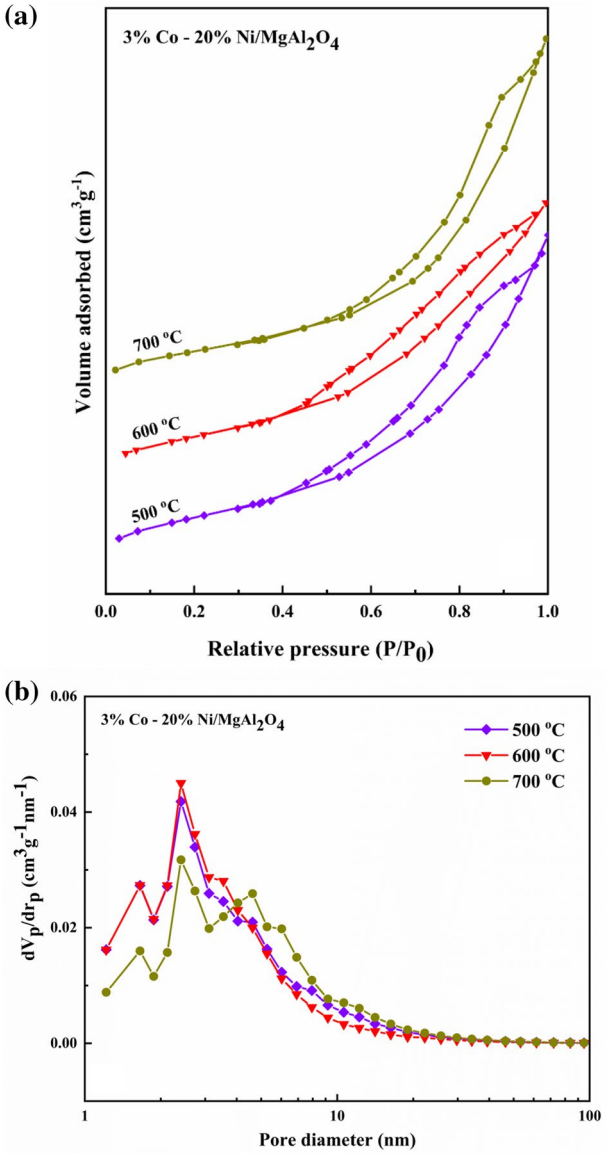

Fig. 15 **a** N_2 adsorption–desorption isotherms and **b** pore size distribution profiles of the 3%Co–20%Ni/$MgAl_2O_4$ catalysts calcined at various temperatures

increased, and the specific surface area decreased. This phenomenon could reduce the catalytic activity [54–57].

Furthermore, the results showed that the prepared samples have a crystallite size in the range of 3.4–3.6 nm. The catalyst crystallinity enhanced with increasing the calcination temperatures from 500 to 700 °C.

Table 3 Structural properties of the 3%Co–20%Ni/$MgAl_2O_4$ catalysts calcined at various temperatures

Calcination temperature (°C)	SBET ($m^2\ g^{-1}$)	Pore volume ($cm^3\ g^{-1}$)	Pore size (nm)	Average crystallite size (nm)
500	91	0.190	8.36	3.4
600	88	0.195	8.82	3.5
700	76	0.226	11.96	3.6

H_2-TPR profiles of the calcined 3%Co-20%Ni/$MgAl_2O_4$ at different temperatures are shown in Fig. 16. Based on this figure, one reduction peak was observed in the range of 700–1000 °C for all samples, which is related to the reduction of nickel oxide species strongly interacted with the $MgAl_2O_4$ phase. The reduction peak in the range of 350–400 °C is correlated with reducing cobalt oxides. As the calcination temperature increased, the interaction between the carrier and base metals became stronger and reduced the reduction capability. Moreover, the cobalt reduction peak in the calcined sample was disappeared at 700 °C. Also, the maximum reduction temperature was shifted to a higher temperature with an increase in calcination temperature from 500–700 °C, which represents the less reducible species at low temperatures.

Figure 17a, b, and c indicated the field emission scanning electron microscopy (FESEM) analysis of the 3%Co-20%Ni/$MgAl_2O_4$ catalysts calcined at 500, 600, and 700 °C. These images confirmed that the catalysts have nanocrystalline structures. In addition, the particle size increased with rising calcination temperatures owing to the sintering of particles at higher temperatures [54].

The influence of calcination temperature on the catalytic performance of different samples in the catalytic oxidation of methane was performed by investigating the conversion rate of methane at different temperatures, Fig. 18. There

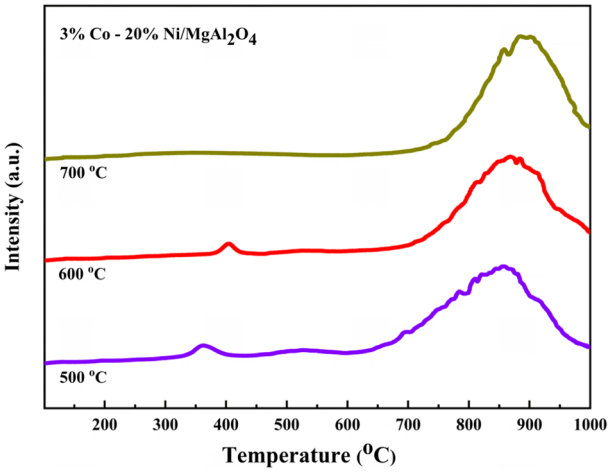

Fig. 16 H_2-TPR profiles of the 3%Co–20%Ni/$MgAl_2O_4$ catalyst calcined at various temperatures

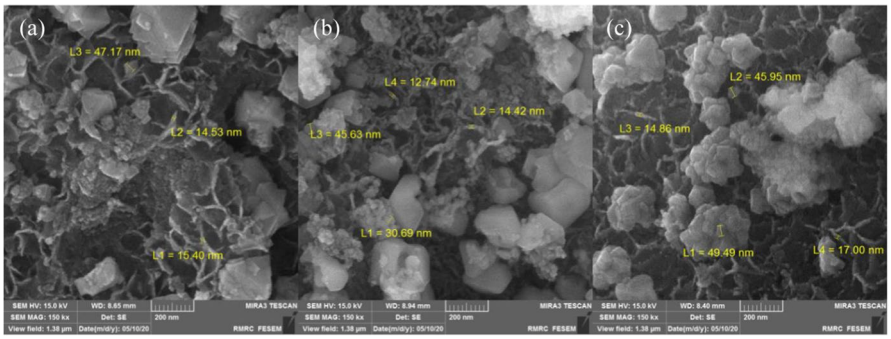

Fig. 17 FESEM images of the 3%Co–20%Ni/$MgAl_2O_4$ catalyst calcined at various temperatures, **a** 500, **b** 600 and **c** 700 °C

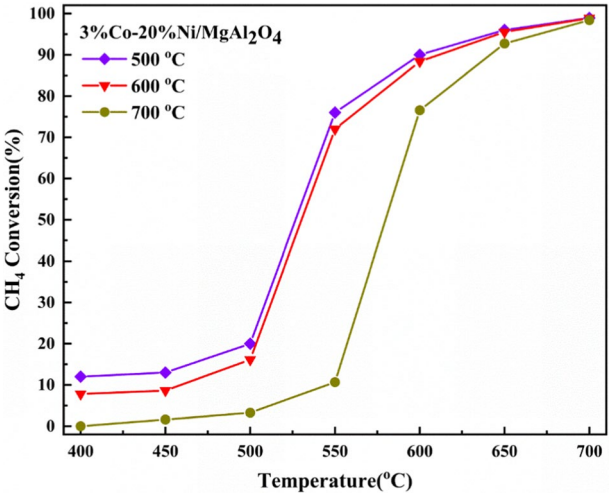

Fig. 18 CH_4 conversion of the 3%Co–20%Ni/$MgAl_2O_4$ catalyst calcined at various temperatures

were no side reactions during the process, and complete oxidation of methane was performed in all samples.

As shown in Fig. 18, the CH_4 conversion reduced with increasing the calcination temperature, which is ascribed to the agglomeration of particles and destruction of mesoporous structure and rise in crystallite size. The calcined 3%Co-20%Ni/$MgAl_2O_4$ at 500 °C showed the highest methane conversion. However, the calcined sample at 700 °C possessed a higher light-off temperature (50 °C) and exhibited a lower methane conversion.

Conclusion

In this study, cobalt oxide was applied as a promoter to enhance the catalytic performance of the 20 wt.% $Ni/MgAl_2O_4$ catalyst. Cobalt was able to cause complete oxidation of methane at all studied operating conditions. However, there was no side reaction and the selectivity to carbon dioxide was equal to one. XRD patterns of the prepared catalysts with constant amounts of nickel and different contents of cobalt showed that increasing the cobalt loading, increased the intensity of peaks related to the Co_3O_4 phase and the average size of nanocrystals. The results of the BET analysis also indicated a high specific surface area for all catalysts. Temperature program analyzes (H_2-TPR and O_2-TPD) showed that the cobalt loading increased the reduction, activation, and oxygen mobility on the catalyst surface. The results of the catalytic tests showed that by increasing the amount of cobalt to 3 wt.%, the catalytic activity improved. However, the addition of higher amounts of cobalt enhanced the particle size and reduced the surface area and number of active sites, which reduced the catalytic performance. Therefore, the catalyst containing 20 wt.% of Ni and 3 wt.% of Co was selected for studying the operation conditions. During the stability test, the presence of magnesium aluminate stabilized the cobalt and nickel oxides and reduced the agglomeration of the particles. Also, FESEM analysis of the used sample showed low agglomeration of the catalyst particles, and no carbon deposition was seen on the catalyst. Increasing the GHSV value increased the methane conversion rate, and increasing the feed ratio (O_2/CH_4) and diluting it with argon decreased the methane catalytic performance. The impact of calcination temperatures on optimal catalyst performance was also investigated. According to the XRD results, the change in calcination temperature did not cause the formation of a new phase in the catalyst. Also, raising the calcination temperature enhanced the crystallite size and reduced the specific surface area. The trend of increasing particle size with raising the calcination temperature in FESEM images indicates these changes. The catalytic tests showed that raising the calcination temperature reduced the catalytic efficiency in methane oxidation.

Acknowledgements The authors gratefully acknowledge the support received from the Iran National Science Foundation (INSF) under the grant number of 97017638.

References

1. B. Durand, EDP Sci. **198**, 101 (2019)
2. M. Zhang, J. Wang, Z. Huang, Int. J. Hydrogen Energy **45**, 20426 (2020)
3. X. Tan, N. Han, H. Chen, L. Su, C. Zhang, Y. Li, Ceram. Int. **47**, 8762 (2021)
4. G. Pio, S. Renda, V. Palma, E. Salzano, J. Loss Prev. Process Ind. **65**, 104151 (2020)
5. J. Chen, H. Arandiyan, X. Gao, J. Li, Catal. Surv. from Asia **19**, 140 (2015)
6. L. He, Y. Fan, J. Bellettre, J. Yue, L. Luo, Renew. Sustain. Energy Rev. **119**, 109589 (2020)
7. H.A. Khan, J. Hao, A. Farooq, Chem. Eng. J. **397**, 125489 (2020)
8. D. Domingos, L.M.T.S. Rodrigues, R. Frety, S.T. Brandao, Combust. Sci. Technol. **186**, 518 (2014)
9. J. Yang, Y. Guo, Chinese Chem. Lett. **29**, 252 (2018)

10. H. Arandiyan, S.S. Mofarah, C.C. Sorrell, E. Doustkhah, B. Sajjadi, D. Hao, Y. Wang, H. Sun, B.-J. Ni, M. Rezaei, Z. Shao, T. Maschmeyer, Chem. Soc. Rev. **50**, 10116 (2021)
11. W. Huang, W. Zha, D. Zhao, S. Feng, Solid State Sci. **87**, 49 (2019)
12. M. Tian, X.D. Wang, T. Zhang, Catal. Sci. Technol. **6**, 1984 (2016)
13. L. Zhong, Q. Fang, X. Li, Q. Li, C. Zhang, G. Chen, Appl. Catal. A Gen. **579**, 151 (2019)
14. P.J. Jodłowski, R.J. Jędrzejczyk, D. Chlebda, M. Gierada, J. Łojewska, J. Catal. **350**, 1 (2017)
15. S. Zhang, J. Shan, L. Nie, L. Nguyen, Z. Wu, F. Tao, Surf. Sci. **648**, 156 (2016)
16. F. Yu, X. Xu, H. Peng, H. Yu, Y. Dai, W. Liu, J. Ying, Q. Sun, X. Wang, Appl. Catal. A Gen. **507**, 109 (2015)
17. D. Qiao, G. Lu, D. Mao, Y. Guo, Y. Guo, J. Mater. Sci. **46**, 641 (2011)
18. D. Li, R. Xu, M. Tian, Y. Jia, Z. Gu, X. Zhu, K. Li, Appl. Therm. Eng. **181**, 116012 (2020)
19. J. Vazquez-Samperio, G. Ramírez-Campos, M.Á. León-Luna, F. Echevarría, A. Cano, A. Hernández-Gordillo, P. Acevedo-Peña, E. Reguera, Electrochim. Acta **380**, 138218 (2021)
20. R.R. Samal, A.K. Samantara, S. Mahalik, J.N. Behera, B. Dash, K. Sanjay, New J. Chem. **45**, 2795 (2021)
21. M.S. Morassaei, A. Salehabadi, O. Amiri, M. Salavati-Niasari, A. Akbari, J. Alloys Compd. **858**, 158374 (2021)
22. Y. Zheng, Y. Yu, H. Zhou, W. Huang, Z. Pu, RSC Adv. **10**, 4490 (2020)
23. M.A. Ulla, R. Spretz, E. Lombardo, W. Daniell, H. Knözinger, Appl. Catal. B Environ. **29**, 217 (2001)
24. T. Xiao, S. Ji, H. Wang, K.S. Coleman, M.L.H. Green, J. Mol. Catal. A Chem. **175**, 111 (2001)
25. L.F. Liotta, G. Di Carlo, G. Pantaleo, A.M. Venezia, G. Deganello, Appl. Catal. B Environ. **66**, 217 (2006)
26. Z. Shi, Q. Zhao, B. Guo, T. Ji, H. Wang, Mater. Des. **193**, 108858 (2020)
27. A.Z. Senseni, F. Meshkani, S.M.S. Fattahi, M. Rezaei, Energy Convers. Manag. **154**, 127 (2017)
28. G.B. Nuernberg, E.L. Foletto, L.F.D. Probst, N.L.V. Carreño, M.A. Moreira, J. Mol. Catal. A Chem. **370**, 22 (2013)
29. M. Rezaei, S.M. Alavi, Int. J. Hydrogen Energy **44**, 16516 (2019)
30. A.H. Khoja, M. Anwar, S. Shakir, M.T. Mehran, A. Mazhar, A. Javed, N.A.S. Amin, Res. Chem. Intermed. **46**, 3817 (2020)
31. A.A. Fard, R. Arvaneh, S.M. Alavi, A. Bazyari, A. Valaei, Int. J. Hydrogen Energy **44**, 21607 (2019)
32. R. Arvaneh, A.A. Fard, A. Bazyari, S.M. Alavi, F.J. Abnavi, Korean J. Chem. Eng. **36**, 1033 (2019)
33. M. Luneau, E. Gianotti, N. Guilhaume, E. Landrivon, F.C. Meunier, C. Mirodatos, Y. Schuurman, Ind. Eng. Chem. Res. **56**, 13165 (2017)
34. H. Li, R. Fu, W. Duan, Z. Jiang, J. Environ. Chem. Eng. **4**, 2187 (2016)
35. E. Akbari, S.M. Alavi, M. Rezaei, J. CO2 Util. **24**, 128 (2018)
36. F. Meshkani, S.F. Golesorkh, M. Rezaei, M. Andache, Res. Chem. Intermed. **43**, 545 (2017)
37. S. Nam, M. Lee, B.N. Kim, Y. Lee, S. Kang, Ceram. Int. **43**, 15352 (2017)
38. N. Habibi, Y. Wang, H. Arandiyan, M. Rezaei, Adv. Powder Technol. **28**, 1249 (2017)
39. L. Yang, Q. Meng, N. Lu, G. He, J. Li, Ceram. Int. **45**, 7635 (2019)
40. Y. Hao, Y. Zhang, S. Wang, Inorg. Chem. Commun. **132**, 108853 (2021)
41. Y.G. Mateyshina, D.V. Alekseev, V.R. Khusnutdinov, N.F. Uvarov, Mater. Today Proc. **12**, 13 (2019)
42. S. Çetintaş, U. Yildiz, D. Bingöl, J. Clean. Prod. **199**, 616 (2018)
43. E. Akbari, S.M. Alavi, M. Rezaei, Fuel **194**, 171 (2017)
44. M.N. Barroso, A.E. Galetti, M.C. Abello, Appl. Catal. A Gen. **394**, 124 (2011)
45. M. Rezaei, S.M. Alavi, S. Sahebdelfar, P. Bai, X. Liu, Z.F. Yan, Appl. Catal. B Environ. **77**, 346 (2008)
46. A. Biabani-Ravandi, M. Rezaei, Chem. Eng. J. **184**, 141 (2012)
47. M. Zarei, F. Meshkani, M. Rezaei, Adv. Powder Technol. **27**, 1963 (2016)
48. K.Y. Koo, H.S. Roh, Y.T. Seo, D.J. Seo, W.L. Yoon, S.B. Park, Int. J. Hydrogen Energy **33**, 2036 (2008)
49. A.H. Braga, D.C. De Oliveira, A.R. Taschin, J.B.O. Santos, J.M.R. Gallo, J.M.C. Buen, ACS Catal. **11**, 2047 (2021)
50. E. Akbari, S.M. Alavi, M. Rezaei, A. Larimi, Int. J. Hydrogen Energy **46**, 5181 (2021)
51. W. Liu, Y. Xu, Z. Tian, Z. Xu, J. Nat. Gas Chem. **12**, 237 (2003)
52. R. Burch, P.K. Loader, Appl. Catal. B Environ. **5**, 149 (1994)

53. Z. Wang, J. Deng, Y. Liu, H. Yang, S. Xie, Z. Wu, H. Dai, Catal. Today **281**, 467 (2017)
54. A. Rastegarpanah, F. Meshkani, M. Rezaei, Int. J. Hydrogen Energy **42**, 16476 (2017)
55. A. Biabani-Ravandi, M. Rezaei, Z. Fattah, Process Saf. Environ. Prot. **91**, 489 (2013)
56. R. Jokar, S.M. Alavi, M. Rezaei, E. Akbari, Int. J. Hydrogen Energy **46**, 32503 (2021)
57. K. Tamimi, S.M. Alavi, M. Rezaei, E. Akbari, J. Energy Inst. **99**, 48 (2021)